

13 QCL-based Gas Sensing with Photoacoustic Spectroscopy

Vincenzo Spagnolo, Pietro Patimisco, Angelo Sampaolo, and Marilena Giglio

Polytechnic University of Bari, Italy

13.1 Overview on Optical Gas Sensing

Gas detection has a great impact in a wide range of applications. For example, the use of high-sensitivity gas detectors is widespread in atmospheric science, to measure and study the profile and pathways of different gas species, including greenhouse gases. Gas sensing finds applications also in medicine and life sciences, mostly for breath analysis: various potential biomarker gases are under study for use in human breath diagnostics, including nitric oxide (NO), ethane (C₂H₆), ammonia (NH₃), carbon oxide (CO), and many others.

Quantitative detection of gases is traditionally performed by laboratory analytical equipment such as gas chromatographs and mass spectrometers, or by small low-cost devices such as pellistors, semiconductor gas sensors, or electrochemical devices. Pellistors are four-terminal devices based on a Wheatstone bridge circuit which includes two beads: one of these beads is treated with a catalyst, which lowers the ignition temperature of explosive gases. The heating coming from combustion events changes the conductivity of the catalyst-treated bead, resulting in an imbalanced voltage, from which the gas concentration can be retrieved [1]. However, pellistors suffer from drift at parts per million (ppm) levels and can be subjected to poisoning, i.e., a change (partially reversible or irreversible) in sensor response due to chemical reactions between certain gases with the catalyst surface. Semiconductor gas sensors possess an electrical resistance made with a porous assembly of tiny crystals of an n-type metal oxide semiconductor (MOS), typically SnO₂, In₂O₃, or WO₃. The resistance value changes sharply on contact with a small concentration of reducing or oxidizing gas, enabling the gas concentration to be related to the resistance change [2]. However, these types of sensors also suffer from drift, cross-talking with other gases, and from changes of humidity levels. Electrochemical gas sensors are based on the electro-adsorptive effect, where electrical fields applied on the gas-sensitive layer may alter the adsorption characteristics of the material. They can be specifically related to individual gases and are sensitive up to the parts per billion (ppb) concentration level; however, they have limited lifetimes and suffer from cross-response issues.

Gas sensors based on optical absorption offer fast responses times (usually below 1 second), minimal drift and high gas specificity, and, in most cases, have zero cross-response to other gases. Measurements can be performed in real time and in situ without altering the gas sample, which can be important for industrial process control. The detection is based on the direct or indirect measurement of the target molecules' absorption at a specific wavelength. Each gas species is characterized by specific

absorption lines or bands, thus guaranteeing the high selectivity of single gas species detection [3]. Many molecular species exhibit strong absorption in the infrared region, where roto-vibrational transitions occur. The excitation of these transitions provides a highly sensitive tool for specific recognition of gas molecules. For mid-infrared optical sources, quantum cascade lasers (QCLs) are the optimal choice, due to their high output power, compactness, narrow spectral linewidth, and broad wavelength tunability. Among laser-based techniques, photoacoustic (PAS) spectroscopy is an indirect technique in that an effect of optical absorption is measured rather than the absorption itself [4]. When light at a specific wavelength is absorbed by the gas sample, the excited molecules will subsequently relax through non-radiative processes. These processes produce localized heating in the gas, which in turn results in an increase in the local pressure. PAS can detect weak acoustic waves and local heating in a gas sample, respectively, and is capable of reaching concentration levels down to the part-per trillion range and below [5] with a compact and robust detection module.

13.2 Introduction on the Photoacoustic Effect

The photoacoustic effect was observed by Graham Bell more than a century ago (1880) while he was working on the improvement of a photophone, in an accidental way. Bell realized that when a light beam is periodically interrupted by a chopper and subsequently focused on a layer of thin material (a diaphragm in connection with an acoustic horn) a sound wave is produced. In addition, the generated acoustic signal increased in intensity when the layer exposed to the beam was dark in color. Thus, Bell realized that this effect was related to the absorption of light by the thin layer. The photoacoustic effect occurs in all kind of materials (solids, liquids, and gases) and scientists began to study the phenomenon and its possible applications [6]. However, due to the lack of appropriate equipment (such as light sources, microphones), the photoacoustic effect was completely forgotten for more than half a century.

The photoacoustic effect for gas species can be divided into three main processes that can be analysed separately:

- generation of heat in the gas as a consequence of the absorption of the modulated optical radiation;
- generation of the acoustic wave;
- detection of the photoacoustic signal.

In Fig. 13.1 the main processes that take place in the production of thermal effects are sketched.

In the following subsections, a detailed description of these three steps is presented.

13.2.1 Absorption of Modulated Light and Generation of Heat

When modulated light is absorbed by molecules via resonant absorption processes, the optically excited molecules may transfer the excess energy to the neighbored molecules by non-radiative collision processes. The absorption of a photon causes a

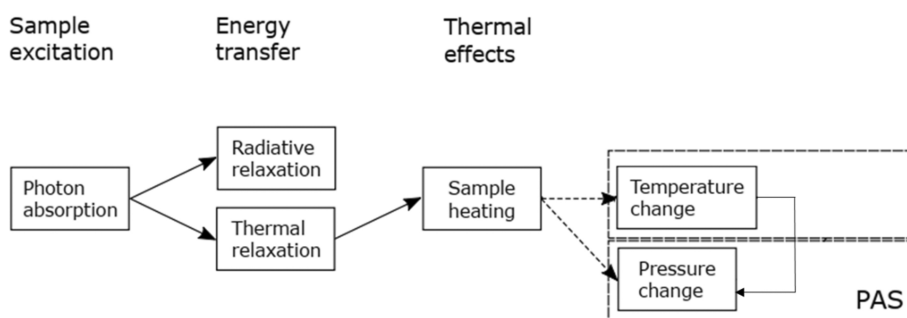


Fig. 13.1 Processes that involve the generation of thermal effects in a gas sample.

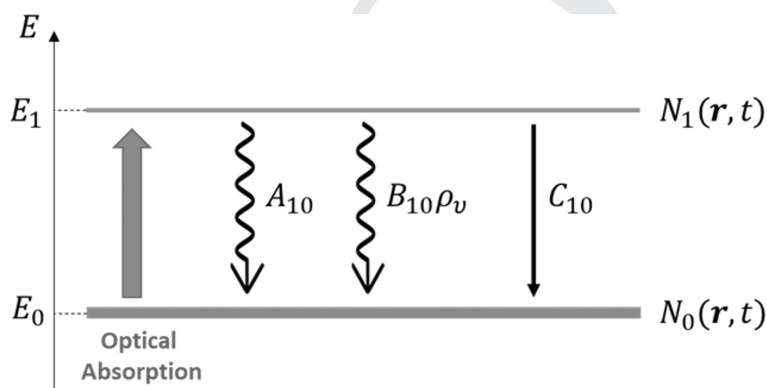


Fig. 13.2 Radiative and nonradiative transitions for a two-level system.

transition from the molecule fundamental energy state E_0 to the excited one E_1 , being $E_1 - E_0 = h\nu$ the energy of the photon and ν its frequency. Then, the molecule relaxes to the fundamental state via different relaxation processes:

- radiative relaxation with the emission of a photon;
- photochemical processes;
- collisions with neighbored molecules of same species at the fundamental energy E_0 with a consequent excitation at the level E_1 ;
- collisions with other type of gas molecules with transfer of the vibrational energy of excited analytes into kinetic energy (translation) of the surrounding molecules (V-T relaxation), causing an increase of the local temperature.

When the optical absorption occurs in the infrared spectral range, the roto-vibrational energy states are involved. Typical non-radiative relaxation times at pressure below 1 bar are of the order of 10^{-6} – 10^{-9} s, while radiative decay times are between 10^{-1} – 10^{-3} s. In addition, energies of the infrared photons are too small to induce chemical reactions. Thus, the absorbed optical energy is mainly released as heat because of the increase of kinetic energy of collided molecules.

Let us suppose that the absorption process in a gas can be schematized as a two-level system, as sketched in Fig. 13.2.

$N_0(\mathbf{r}, t)$ and $N_1(\mathbf{r}, t)$ are molecular density for the fundamental energy state E_0 and the excited energy state E_1 , respectively, ρ_ν is the energy density of radiation, A_{10} and B_{10} are the Einstein coefficient for spontaneous emission and stimulated emission, respectively, and C_{10} is the non-radiative transfer rate via collisions. The rate equation for the population $N_1(\mathbf{r}, t)$ can be expressed as:

$$\frac{dN_1}{dt} = \rho_\nu B_{10} (N_0 - N_1) - (A_{10} + C_{10}) N_1. \quad (13.1)$$

The inverse of lifetime τ of the excited state can be expressed as $1/\tau = A_{10} + C_{10}$ and, in a weak optical absorption approximation, namely $N_1 \ll N_0$ and N_0 time-independent, the previous equation can be rewritten as:

$$\frac{dN_1}{dt} = \rho_\nu B_{10} N_0 - \frac{N_1}{\tau}. \quad (13.2)$$

The term $\rho_\nu B_{10}$ represents the absorption optical rate and can be expressed as the product between the photon flux and absorption cross-section σ . When the photon flux is modulated at a frequency ω it can be expressed as:

$$F(\mathbf{r}, t) = F_0(\mathbf{r}) (1 + \delta e^{i\omega t}). \quad (13.3)$$

When $\delta \ll 1$, a small amplitude sinusoidal modulation is superimposed to a time-independent photon flux $F_0(\mathbf{r})$. By combing Eqs. (13.2) and (13.3), the differential equation can be solved, and the density of the excited molecules can be related to the optical absorption of modulated light:

$$N_1(\mathbf{r}, t) = \frac{N_0 \sigma F_0(\mathbf{r}) \delta}{\sqrt{1 + \omega^2 \tau^2}} \tau e^{i(\omega t - \vartheta)}, \quad (13.4)$$

where ϑ is the phase difference between the modulation of the population density and the photon flux. The heat rate generated by the optical absorption can be related with the population density:

$$H(\mathbf{r}, t) = \frac{N_1(\mathbf{r}, t) \cdot h\nu}{\tau} = \frac{N_0 \sigma F_0(\mathbf{r}) \delta h\nu}{\sqrt{1 + \omega^2 \tau^2}} e^{i(\omega t - \vartheta)}, \quad (13.5)$$

where $h\nu = E_1 - E_0$ is the energy of the absorbed photon. The product $N_0 \sigma$ represents the absorption coefficient of the optical transition and it is proportional to the gas target concentration. This model requires two assumptions: (i) $F_0(\mathbf{r}) \sigma$ should be low in order to avoid absorption saturation and neglect stimulated emission; and (ii) low-frequency modulation, $\omega \ll 1/\tau$. The first condition is verified for low concentrations of absorbing gas and the second one by keeping the modulation frequency in the kHz range.

13.2.2 Generation of Acoustic Waves

The generation of the acoustic wave is related to the local periodic variation of the pressure as a consequence of the periodic heating of the sample due to the non-radiative energy relaxation of absorbing gas. The theoretical model is based on a combination of fluid mechanics and thermodynamics laws. We consider the case of an

ideal, uniform, and continuous fluid that is perfectly elastic and at the thermodynamic equilibrium except for the local variations produced by the pressure wave, which are small enough to neglect any non-linear effects. The effect of the gravitational force is also neglected, so that pressure and the density at equilibrium can be considered constant throughout the fluid. Dissipative terms due to fluid viscosity are not considered in the model. The propagation of the acoustic wave produces local changes in pressure, density, and temperature in the gas, proportional to the acoustic wave amplitude. Pressure changes are easily measured by means of sound detectors. For this reason, the acoustic wave is usually described in terms of acoustic pressure, which is defined as the difference between the instantaneous pressure and the equilibrium pressure. The equations that rule the acoustic pressure p are (i) the ideal gas law:

$$\frac{p}{\rho} = (\gamma - 1) \frac{C_V}{M} T, \quad (13.6)$$

where ρ is the gas density, γ is the ratio between the specific heat for the ideal gas at constant pressure (C_p) and at constant volume (C_V), M is the molar mass, and T is the temperature; (ii) the continuity equation:

$$-\frac{1}{\rho} \frac{\partial p}{\partial t} = \nabla \cdot \mathbf{v}, \quad (13.7)$$

where \mathbf{v} is the velocity field; (iii) the law of momentum conservation:

$$\rho \frac{\partial \mathbf{v}}{\partial t} = -\nabla p, \quad (13.8)$$

and (iv) the conservation of energy:

$$\rho \frac{C_V}{M} \frac{\partial T}{\partial t} + p \nabla \cdot \mathbf{v} = H. \quad (13.9)$$

By combining Eqs. (13.6)–(13.9), it can be demonstrated that the acoustic pressure is governed by the D'Alembert wave equation:

$$\nabla^2 p(\vec{r}, t) - \frac{1}{c^2} \frac{\partial^2 p(\vec{r}, t)}{\partial t^2} = -\frac{\gamma - 1}{c^2} \frac{\partial H}{\partial t}, \quad (13.10)$$

where:

$$c = \sqrt{\frac{\gamma RT}{M}} \quad (13.11)$$

is the speed of sound in the gas. Since H is sinusoidally modulated, it is convenient to take the Fourier transform of Eq. (13.10), considering \mathbf{r} as a parameter:

$$\left(\nabla^2 + \frac{\omega^2}{c^2} \right) p(\mathbf{r}, \omega) = \frac{\gamma - 1}{c^2} i\omega H(\mathbf{r}, \omega). \quad (13.12)$$

A general solution $p(\mathbf{r}, \omega)$ can be expressed as infinite summation of acoustic modes $p_k(\mathbf{r})$:

$$p(\mathbf{r}, \omega) = \sum_k A_k(\omega) p_k(\mathbf{r}), \quad (13.13)$$

where $A_k(\omega)$ is the amplitude of the k -th acoustic mode with angular frequency ω_k and $p_k(\mathbf{r})$ is the solution of the associated homogeneous equation.

13.2.3 Detection of Acoustic Waves

In photoacoustic spectroscopy, the gas is enclosed within an acoustic cell where optical absorption takes place [4]. The calculation of the normal acoustic modes of the gas cell is determined by imposing boundary conditions, dependent on the geometry of the acoustic cell. Most common acoustic cell designs adopt the basic symmetry of the exciting light source and are cylindrically shaped. The excitation source is a small diameter light beam centered along the cylinder axis. Local pressure propagates radially outward perpendicular to the exciting beam. The resonances occur at frequencies f_{res} and for a cylindrical acoustic cell of length L and radius R , it is given by [7]:

$$f_{\text{res}} = \frac{c}{2} \sqrt{\left(\frac{k}{L}\right)^2 + \left(\frac{\alpha_{m,n}}{R}\right)^2}, \quad (13.14)$$

where k , m , and n are indices related to the longitudinal, azimuthal, and radial acoustic modes, and $\alpha_{m,n}$ are determined by boundary conditions. Numerical values for the lowest order roots are: $\alpha_{0,0} = 0$, $\alpha_{0,1} = 1.226$, and $\alpha_{1,0} = 0.5891$. For air ($c = 3.31 \times 10^4 \text{ cm s}^{-1}$) in a cell with a diameter of 5 cm and a length of 15 cm, the lowest resonance frequencies are 1.1 kHz for the longitudinal ($k = 1, m = n = 0$) mode, 3.9 kHz for the azimuthal ($m = 1, k = n = 0$) mode, and 8.1 kHz for the radial ($n = 1, k = m = 0$) mode.

When the radiation modulation frequency matches the resonance frequency of the acoustic cell, i.e., $\omega = 2\pi f_{\text{res}}$, a standing wave vibrational pattern is created within the acoustic cell which acts as an acoustic resonator. In other words, cell resonances enhance and amplify acoustic powers at the resonance frequency. The degree of amplification of an acoustic cell is described by a quantity called the quality factor Q . Q values of more than 1000 have been reported and values of a few hundred are typical for a radial resonance mode. Due to the cylindrical symmetry, longitudinal (and azimuthal) modes are not as strongly excited and have somewhat lower Q values compared to the radial mode. The amplitude of the acoustic mode at the resonance frequency f_{res} is proportional to:

$$A_k(f_{\text{res}}) \propto \frac{\alpha PLQ}{f_{\text{res}} V}, \quad (13.15)$$

where P is the radiation power and V is the cell volume. Geometries other than cylindrical symmetry have also been employed. Cells that exploit Helmholtz resonances are constructed with two chambers, a sample chamber of volume V_1 and a microphone chamber of volume V_2 , connected by a cylindrical tube of length l and inside diameter D [8]. The resonance frequency exhibited by such cells is given by the expression:

$$f_{\text{res}} = \frac{Dc}{2\sqrt{\pi}} \sqrt{\frac{V_1 + V_2}{V_1 V_2 (l + \frac{\pi D}{2})}}. \quad (13.16)$$

From Eq. (13.16), the resonance frequency is reduced if a long narrow tube is used between the two cell chambers.

Several devices can be used to detect the sound wave generated by sample absorption. Most photoacoustic experiments utilize pressure sensors, the most common of which are microphones. A condenser microphone produces an electrical signal when a pressure wave impinging on the diaphragm pushes the diaphragm closer to a fixed metal plate, thereby increasing the capacitance between these two surfaces. The capacitance change leads to a voltage signal which increases with bias voltage and the diaphragm area. Microphones generally have flat frequency response up to 15 kHz, have low distortion, are generally not sensitive to mechanical vibrations, and respond well to pressure impulses, which enables their use in pulsed applications [9]. The dielectric material between the condenser plates in this type of microphone is air. In contrast to condenser microphones, electret microphones are constructed using solid materials of high dielectric constant which are electrically polarized [10]. One side of the electret foil is metallized and the insulating side is placed on a fixed back plate. A sound wave impinging on the metallized side causes a change in the polarization characteristics of the electret material, which in turn produces a small voltage between the metallized front electret surface and the back plate of the microphone. Thus, an electret microphone requires no bias voltage, which simplifies the apparatus. Another striking difference between air-spaced condenser microphones and electret microphones is physical size. Due to the large capacitance per unit area possible from electret materials they can be made into miniaturized microphones.

The need for windows on the acoustic cell affects its performance in two ways. Brewster windows, for example, destroy the cylindrical shape, which tends to dampen the natural acoustic resonances of the cell. Consequently, cell Q factors are lowered somewhat by the presence of these windows. Windows also generate a background acoustic signal at the source modulation frequency which can interfere with the detection of weak acoustic signals. Background acoustic signals are due to light absorption or scattering by the window material itself or from dust or adsorbed sample molecules on the window surface. The resultant window heating is transferred to the gas sample, generating an acoustic signal. Several cell designs, such as the use of baffles, for example, have been partially successful in minimizing cell window backgrounds. Different designs for PAS cells have been proposed and implemented, including a resonant cell with acoustic buffers [11], windowless [12], and a differential cell [13]. A differential cell includes two acoustic resonators equipped with microphones having the same responsivity at the resonance frequency of the cell. Since the laser light excites only one of the two resonators, the difference between the two signals removes noise components that are coherent in both resonators.

Optical microphones based on an interferometric displacement concept have been also employed in PAS [14]. Their design utilizes an interferometric technique whereby a metal coated 50/50 transmission diffraction grating is integrated in the middle of the acoustic backcavity. Together with the metal-coated acoustic diaphragm, a Michelson interferometer is formed. This approach provides sub-picometer displacement resolution and pressure sensitivity in the low $\mu\text{Pa}/\sqrt{\text{Hz}}$ range. The acoustic resonant

frequency is adjustable from 10 kHz to 100 kHz, depending on membrane stiffness (thickness) and diameter [15].

The highest sensitivity has been achieved by using a cantilever pressure sensor [5] that is over hundred times more sensitive compared to membrane microphones. An extremely thin cantilever portion moves like a flexible door due to the pressure variations in the surrounding gas. The movement of the free end of the cantilever can be about two orders of magnitude greater than the movement of the middle point of the tightened membrane under the same pressure variation. The displacement of the cantilever is measured optically [16].

PAS has been successfully applied in trace gas sensing applications, which include atmospheric chemistry, volcanic activity, agriculture, industrial processes, workplace surveillance, and medical diagnostics. For instance, PAS has been used to monitor nitric oxide (NO) from vehicle exhaust emissions, which contributes to respiratory allergic diseases, inflammatory lung diseases, bronchial asthma, and the depletion of ozone [17]. In medicine, PAS has been used to monitor drug diffusion rates in skin [18] and to detect trace concentrations of disease biomarkers, such as ethylene (C_2H_4), ethane (C_2H_6), and pentane (C_5H_{12}), which are emitted by UV-exposed skin [19]. Other applications include monitoring respiratory NH_3 emission from cockroaches as well as detecting the intake of prohibited substances by athletes [20]. Low-cost portable PAS sensors have been on the market, examples of which include smoke detectors, toxic gas monitoring, and oil sensors for monitoring hydrocarbons in water.

13.3 Focus on QEPAS

The main issue suffered by PAS sensors is the sensitivity of the employed microphone for external sound sources. This issue can be solved exploiting the quartz-enhanced PAS (QEPAS) approach. In QEPAS a quartz tuning fork (QTF) is used as a sharply resonant acoustic transducer to detect weak photoacoustic waves, avoiding the use of acoustic gas cells, thereby removing restrictions imposed on the gas cell design by the acoustic resonance conditions [21, 22]. The laser beam is focused between the prongs of the QTF and the sound wave generated between them causes an antisymmetric vibration of the prongs in the QTF plane, with the two prongs moving in opposite directions at the same time: as a result, a flexural mode is excited. This vibration mode is piezoelectrically active and thus electrical charges are generated, proportional to the sound wave intensity. The most important advantages of QEPAS are [23]: (1) a high resonance frequency of the tuning fork combined with narrow bandwidth, yielding a very high $Q > 10,000$; (2) applicability over a wide range of pressures, including atmospheric pressure; (3) sample volumes as low as a few cm^3 ; and (4) QTFs are not spectrally sensitive and practically unaffected by environmental noise. Indeed, external acoustic sources tend to apply a force in the same direction on the two QTF prongs (in-plane symmetric mode) and the resulting deflection of QTF prongs is not piezoelectrically active. Thus, in contrast with the antisymmetric vibration of QTF produced by the laser beam, most of the external environmental noise does not generate an electrical signal.

For a harmonic modulation at frequency f of the photon flux, the frequency-dependent generated QEPAS signal at the modulation frequency f can be obtained by revising Eq. (13.15) [24]:

$$S = KQ(P) P_L c \varepsilon(f, \tau) = \frac{KQ(P) P_L c}{\sqrt{1 + (2\pi f \tau)^2}}, \quad (13.17)$$

where K is a sensor constant, P_L is the laser power, c is the analyte concentration, and $\varepsilon(f, P)$ is the radiation-to-sound conversion efficiency, given by [25]:

$$\varepsilon(f, \tau) = \frac{1}{\sqrt{1 + (2\pi f \tau)^2}}. \quad (13.18)$$

For instantaneous relaxation, i.e., $2\pi f \tau \ll 1$, $\varepsilon(f, P) = 1$ and the QEPAS signal will be not dependent on the modulation frequency. According to the Landau–Teller model [26], the dependence of the relaxation time on the gas pressure can be expressed by:

$$\tau = \frac{1}{kP}, \quad (13.19)$$

where k is a constant.

A crucial aspect in QEPAS detection is the dependence of the QEPAS signal on the radiation-to-sound conversion efficiency, which in turn affects the acoustic wave generation within the gas. It is mainly determined by the transfer rate of the vibrational energy of excited analyte molecules into kinetic energy (translation) of the surrounding molecules (V-T relaxation) [27]. The use for several years of standard QTFs operating at frequencies as high as 32.7 kHz in QEPAS sensors has divided the gas species into two categories: fast and slow relaxing gases. For slow relaxing gases, a laser modulation frequency of 32.7 kHz is higher than the effective analyte relaxation rate in the gas matrix, not ensuring a complete release of absorbed energy during each oscillation period. The realization of custom QTFs with resonance frequencies lower than 32.7 kHz paved the way for the detection of slow relaxing molecule concentrations with better sensitivity [28–31]. Conversely, for fast relaxing gases, the relaxation rate is significantly faster than that of the optical modulation and an efficient energy transfer occurs between absorbing analytes and surrounding molecules. Thus, fast relaxing gases (such as H₂O and SF₆) have been used also as relaxation promoters for slow relaxing gases to enhance the detection sensitivity of the latter [32, 33]. In this case, the effective relaxation rate of the analyte depends on the gas matrix composition. Indeed, excited analyte molecules can relax on different channels through collisions with the different types of molecules composing the matrix, both the buffer and the promoter. The relaxation rate is then given by the sum of the relaxation rates of every possible energy transfer pathway, weighted by the concentration of each species in the mixture [34]. Since for slow relaxing gases, the QEPAS signal is dependent on the promoter concentration within the mixture, accurate measurements of the promoter concentration and additional sensor calibration are required. To overcome this issue, custom QTFs with low resonance frequencies (<32.7 kHz) have been realized for QEPAS sensing.

13.3.1 Quartz Tuning Forks

The QTF represents the core of any QEPAS sensor. A tuning fork can be considered as two cantilever bars (prongs) joined at a common base. The in-plane flexural modes of vibrations of the QTFs can be classified into two groups: symmetric modes, in which case the prongs move along the same direction; and antisymmetric modes, in which case the two prongs oscillate along opposite directions. The in-plane antisymmetric modes will be the predominant modes when a sound source is positioned between the prongs, forcing them to move in the opposite directions. In QEPAS sensors, the light source (typically a laser) is focused between the QTF prongs and sound waves produced by the modulated absorption force the prongs to vibrate antisymmetrically back and forth. QTFs can be designed to resonate at any frequency in the 3–200 kHz range and beyond, since resonance frequencies are defined by the properties of the piezoelectric material and by its geometry [28, 35].

The interaction between the laser modulated beam and absorbing molecules leads to the generation of acoustic waves that mechanically bend the QTF prongs. Hence, the electrode pairs of the QTF will be electrically charged due to the quartz piezoelectricity. Piezoelectricity is the coupling between internal dielectric polarization and strain, and it is present in most crystals lacking a center of inversion symmetry [36]. When a stress is applied to these materials, it induces a displacement of charge and a net electric field. The effect is reversible: when a voltage is applied across a piezoelectric material, it is accompanied by strain. The resonance frequencies of a QTF flexural mode can be calculated in the approximation of an independent cantilever vibrating in the in-plane modes. Each prong of the tuning fork can be treated as a clamped beam. According to the Euler–Bernoulli approximation, the description of the vibration is given by the following fourth-order differential equation:

$$EI \frac{\partial^4 y(x, t)}{\partial z^4} + \rho A \frac{\partial^2 y(x, t)}{\partial t^2} = 0, \quad (13.20)$$

where E and ρ are the Young's modulus and the volume density of quartz, respectively, $A = LT$ is the cross-sectional area of the beam (where L and T are the prong length and thickness, respectively, see Fig. 13.3(a)), I is the second moment of beam's cross-sectional area, $y(z, t)$ is the prong displacement function, x and y are the directions in the QTF plane, and t is the time. The geometry of a QTF is sketched in Fig. 13.3.

The product EI is usually referred as the flexural rigidity. The latter, together with the cross-sectional area A and the volume density, are assumed to be constant along the whole beam. The Euler–Bernoulli equation can be solved by the separation of variables method. The displacement can be separated into two parts, one is dependent on position and the other one is a function of time. This leads to a simplified differential equation for the x -direction that can be solved by superimposing boundary conditions. The boundary conditions originate from the support of the QTF. The fixed end must have a zero displacement and zero slope due to the clamp, while the free end does not have a bending moment or a shearing force (free-clamped boundary conditions). The related eigenfrequencies f_n are given by the following expression [24]:

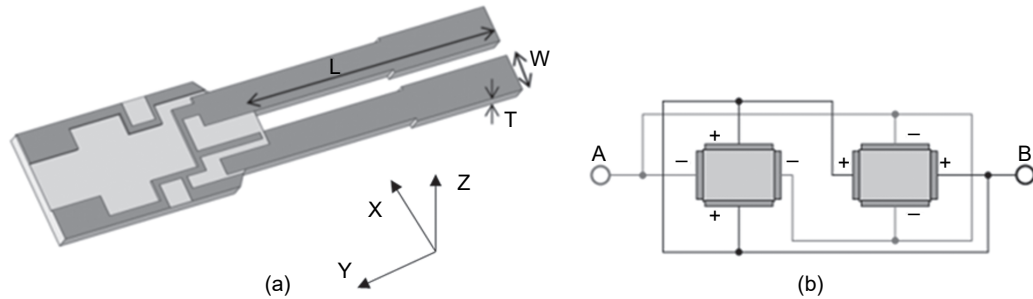


Fig. 13.3 (a) Schematic of a QTF with the reference frame. (b) Top view of the tuning fork with the electrical configuration for the electrodes A and B. As shown, the charges cumulate in a quadrupole configuration.

$$f_n = \frac{\pi T}{8\sqrt{12}L^2} \sqrt{\frac{E}{\rho}} v_n^2, \quad (13.21)$$

where v_n identifies the mode number, i.e., $n=0$ identifies the fundamental flexural mode, $n=1$ the first overtone mode, $n=2$ the second overtone mode, and so on.

13.3.2 Influence of Gas Properties

The dependence of the resonance frequency on the surround gas pressure can be determined by the assumption that the gas effect on prong vibration damping increases the inertia of the prong. In other words, the effect of the surrounding medium can be modeled as an additive mass for the vibrating prong. Thus, the Euler–Bernoulli equation in Eq. (13.20) requires an additional term corresponding to the reactive part, which attributes additional inertia to the vibrating prong [37]:

$$EI \frac{\partial^4 y(z, t)}{\partial z^4} + (\rho A + u) \frac{\partial^2 y(z, t)}{\partial t^2} = 0, \quad (13.22)$$

where u is the added mass per unit length. The eigenfrequency f_u of the fundamental mode changes as:

$$f_u = f_0 \left(1 - \frac{1}{2} \frac{u}{\rho A} \right), \quad (13.23)$$

where f_0 is determined in vacuum by Eq. (13.21) when $n=0$. The exact derivation of the added mass u is a complicated problem even for simple prong structures. In [38], the added mass per unit length of a thin prong has been found to be proportional to gas density ρ_0 . By using the ideal gas law, the gas density can be expressed by $\rho_0 = MP/RT$, where M is molar mass, P is the gas pressure (in torr), $R = 62.3637 \text{ L} \cdot \text{torr} \cdot \text{K}^{-1} \cdot \text{mol}^{-1}$ is the gas constant, and T is the prong temperature (in K). Thus, the QTF resonance frequency shifts linearly with the pressure, if the temperature is assumed to be fixed. The Q-factor of a resonance mode is a measure of the energy loss of the prongs while they are vibrating. It has been demonstrated that the

QTF mainly loses energy via interaction with the surrounding viscous medium. Gas damping is the main loss mechanism for the fundamental and first overtone modes and is proportional to the viscosity and density of the gas. A good approximation for the dependence of the quality factor on the gas pressure is provided by the following equation [39, 40]:

$$Q(P) = \frac{Q_0}{1 + Q_0 b \sqrt{P}}, \quad (13.24)$$

where Q_0 is the quality factor at $P = 0$, which includes all pressure-independent loss mechanisms (support losses and thermoelastic damping), and b is a fitting parameter. Both Q_0 and b are mainly related to QTF geometry and gas viscosity, and thus vary for each QTF.

13.3.3 T-Shaped Grooved Tuning Forks

Moving to low resonance frequencies by varying the ratio T/L following the Euler-Bernoulli equation for rectangular prongs, the Q-factor decreases, as demonstrated in [31]. In particular, QTFs with a resonance frequency lower than 10 kHz cannot ensure $Q > 10,000$ at atmospheric pressure. A further reduction of the resonance frequency without strongly affecting the overall quality factor requires a change of prong geometry. T-shaped prongs have been proposed to accomplish both requirements, with a further increase of stress field distribution along vibrating prongs with respect to rectangular prongs, which is beneficial for piezoelectric charge generation when prongs are deflected. [41–43]. In addition, applying rectangular grooves in prongs increases the electrical coupling between electrodes, leading to a reduction of the electrical resistance without affecting the quality factor [31]. To investigate the resonance properties of a T-shaped grooved QTF, a finite-element-analysis (FEA) using COMSOL Multiphysics was performed. Taking T_1 as the thickness of the T-shaped prong head and T_2 as the thickness of the T-shaped prong body (see Fig. 13.4(a)), the influence of the ratio T_2/T_1 on the resonance frequency was investigated in [44]. T_1 , L_1 , and L_2 were kept constant to 2.0 mm, 2.4 mm, and 7.0 mm, respectively, while T_2 was varied. Grooves 50 μm deep were carved on both sides of each prong, as sketched in Fig. 13.4(b). The simulation was performed in vacuum environment to avoid the influence of the surrounding medium and the results are shown in Fig. 13.4(c). $T_2/T_1 = 0.5$ was set as lower limit for the simulation.

The simulation results clearly indicate a linear trend of the fundamental resonance frequency with respect to the T_2/T_1 ratio, with a R^2 value of 0.9998. Ratios lower than 0.7, i.e., T_1 smaller than 1.4 mm, lead to a resonance frequency lower than 10 kHz. However, the lowering of the resonance frequency through reduction of the T_2/T_1 ratio is in competition with the mechanical stability of the QTF. A low T_2/T_1 ratio would not guarantee a stable oscillation of the QTF prong due to a low moment of inertia. Moreover, prong oscillations would be highly influenced by the surrounding medium damping leading to high viscous losses that in turn negatively affect the quality factor.

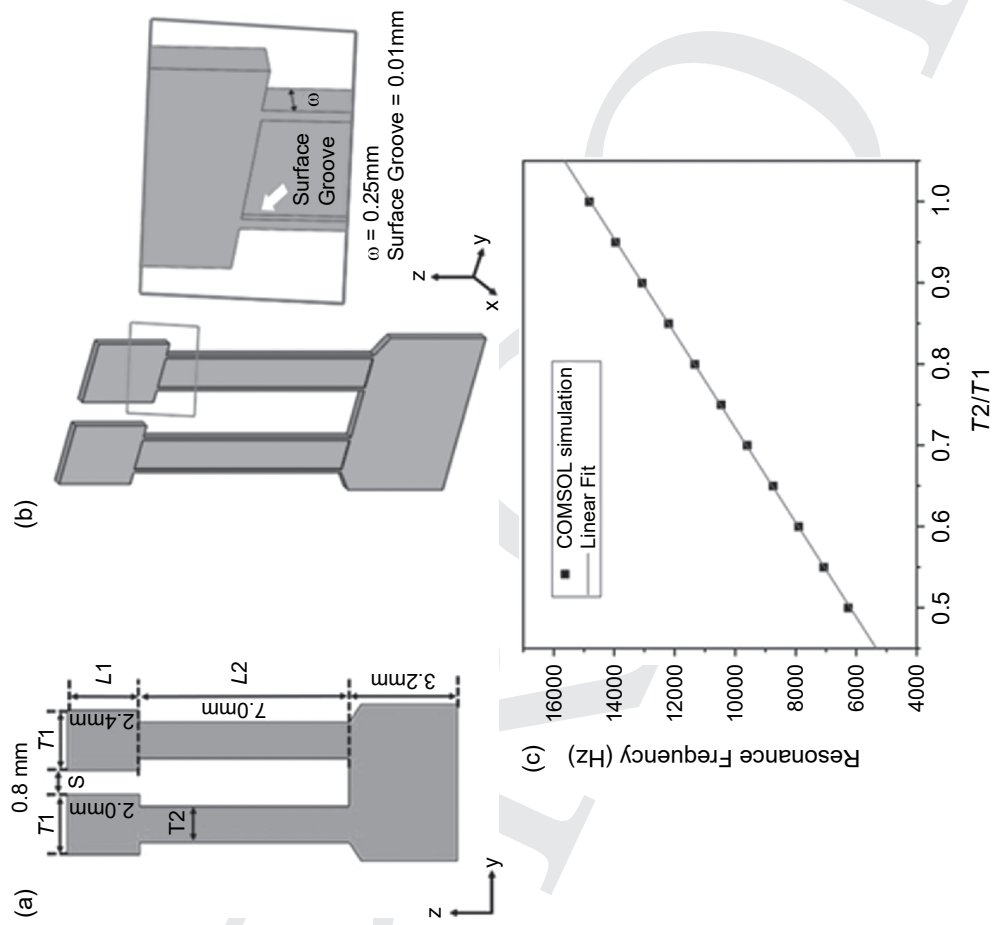


Fig. 13.4 (a) Schematic diagram of the T-shaped grooved QTF, with geometrical parameters shown. (b) Schematic diagram of the grooved prong. (c) Results of COMSOL Multiphysics simulation of fundamental resonance frequency of a T-shaped grooved QTF as a function of the T_2/T_1 ratio when T_1 , L_1 , and L_2 are kept constant to 2.0 mm, 2.4 mm, and 7.0 mm, respectively.

13.3.4 Overtone Modes

The realization of custom-made QTFs optimized for QEPAS applications can significantly improve the sensitivity of the detection technique. With respect to the standard 32.7 kHz QTF, the resonance frequency of the fundamental mode can be reduced to a few kilohertz in order to better approach the typical energy relaxation time of targeted gases [45], while maintaining a high resonator quality factor. Both conditions can be simultaneously satisfied by an appropriate design of the QTF prong sizes [31]. However, lowering the fundamental resonance frequency also reduces the overtone frequencies, leading to their possible use in QEPAS sensor systems. This is not feasible with a 32.7 kHz QTF, since its first overtone mode occurs at frequencies higher than 190 kHz, which is impractical for QEPAS-based gas detection. By using Eq. (13.21), the first overtone mode exhibits a resonance frequency $2.9882/1.1942 \sim 6.26$ times higher than the fundamental mode. This implies that in order to have the first overtone resonance frequency <30 kHz, the fundamental mode must vibrate at frequencies lower than 4.5 kHz. Lowering the operating frequency to values <3 kHz is not recommended in QEPAS since the sensor system would be more influenced by environmental acoustic noise. The fundamental and first overtone modes exhibit different quality factor values because the associated loss mechanisms depend on the related vibrational dynamics and on the geometry of the QTF prongs [39, 46]. Hence, the QTF geometry can be designed to provide an enhancement of the overtone mode resonance Q-factor and thereby a higher QEPAS SNR with respect to the fundamental mode can be expected. According to Hosaka's model [47], the air damping is significantly reduced when moving from the fundamental to overtone mode. However, by moving to higher modes support losses (due to the interaction of the prong with its support) can start to dominate, deteriorating the overall quality factor [48, 49]. An increase of a factor of ~ 12 in support losses is expected for a QTF, when changing from the fundamental to the first overtone mode. The possibility to excite independently and simultaneously both the fundamental and the first overtone flexural mode of a QTF opened the way to simultaneous detection of two different gas species targeted by two different lasers.

13.3.5 Microresonator Tubes

The QTF is not used as a standalone in a QEPAS sensor but it is acoustically coupled with a pair of millimeter-size resonator tubes located on both sides of the QTF, as sketched in Fig. 13.5. This arrangement is known as the on-beam configuration. Conversely, in the off-beam configuration, a single resonator tube is positioned adjacent to the QTF: the QTF senses the pressure in the microresonator through a small aperture in its center [50, 51]. Resonator tubes act as an acoustic resonator: the standing wave vibrational pattern within the tubes enhances the intensity of the acoustic field between the QTF prongs up to 60 times [31]. The QTF coupled with a single or a pair of resonator tubes constitutes the QEPAS spectrophone and represents the core of any QEPAS detection module.

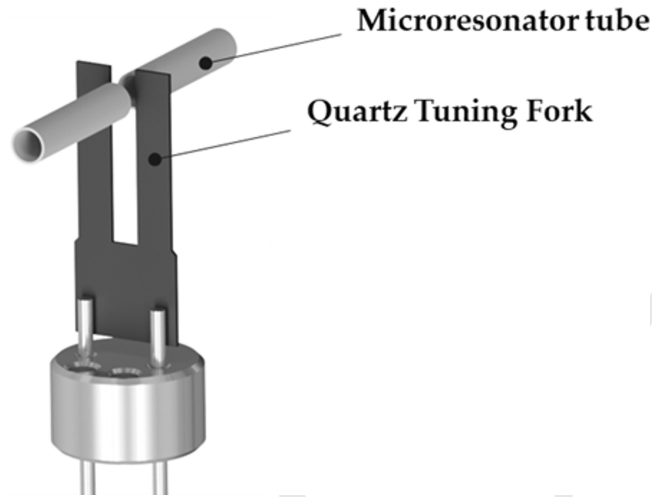


Fig. 13.5 Schematic diagram of the QEPAS spectrometer.

In the on-beam configuration, when two tubes are acoustically coupled with a QTF, the internal diameter (ID) of tubes and their length influence the enhancement of the sound wave between the QTF prongs. The optimal tube diameter can be estimated by considering the theoretical model proposed in [52], in which the acoustic coupling between the two tubes is expressed in terms of the amount of the acoustic field transferred from one tube to the other one. As a result, the optimal tube radius strongly depends on the sound wavelength λ_s and prong spacing g . As an example, for a QTF resonating at 8 kHz in pure SF₆ ($\lambda_s = v_s/f_0 = 16.7$ mm, with $v_s = 136$ m/s being the speed of sound in the SF₆ gas and $g = 800$ μ m) the theoretical model predicts the optimal ID = 1.0 mm. The optimal tube length can be estimated by considering the open-end correction, which assumes that the antinode of a standing sound wave in an open-ended resonator is located outside the tube end, due to an impedance mismatch between the acoustic field inside and outside of the resonator. The optimal tube length l depends on the tube ID and the sound wavelength by the relation [53]:

$$l = \frac{v_s}{2f_0} - \frac{8ID}{3\pi}. \quad (13.25)$$

Thus, the optimal tube length depends on the tube ID, the speed of sound, and the resonance frequency of the acoustic wave. The QTF acoustically coupled with a pair of resonator tubes composes the QEPAS spectrophone, which is the core of the detection module of any QEPAS sensor.

13.4 Overview of QCL-based QEPAS Gas Sensors

High selectivity and detection sensitivity, and short response time are the primary requirements for trace gas sensing. These characteristics, combined with no downtime between data sampling and analysis, no need for frequent recalibration, the absence of any saturable or degradable components, portability, and low cost, are the primary

13 QCL-based Gas Sensing with Photoacoustic Spectroscopy

425

Table 13.1 The list of the main methods and techniques employed in gas analyzer technologies and their characteristics (shaded cells).

Technique	High sensitivity	Short response time	No degradation	Small size	In-situ monitoring	Low cost
GC-MS						
Chemi-luminescence						
Electrochemical-based						
Laser-based						

requirements for a gas sensor system to be particularly suitable for in-field applications like environmental monitoring, breath sensing, leak detection, industrial processes control, and oil and gas exploration. The characteristics of the commonly employed methods in gas analysers, i.e., gas chromatography–mass spectrometry (GC-MS), chemiluminescence, and electrochemical- and laser-based techniques, are summarized in Table 13.1.

Although the peaks in the GC-MS technique allow unambiguous identification of gas components with a very high sensitivity, the gas chromatography columns and mass spectrometers are bulky, expensive, and do not allow for in-situ measurements [54]. When dealing with chemiluminescence-based analysers, instability over time and the need for daily calibration must be added to these drawbacks [55]. Electrochemical-based analysers are inexpensive and very small, making them suitable for compact devices. However, these sensors exhibit a lower response time and a lower sensitivity, compared to the other techniques, and a reliability degradation over time [56]. Finally, laser-based analysers (LAs) can provide highly sensitive and selective detection, with fast response time [57]. Mid-infrared QCLs are perfect excitation sources for laser-based gas sensor systems due to their operation in the spectral range covering most of the fundamental gas absorption lines with single-mode relatively narrow linewidth emission, fulfilling the selectivity requirement [58]. Compared to other laser sources, QCLs have high optical power output which leads to higher achievable sensitivity in QEPAS sensors and can be implemented in a distributed-feedback or external-cavity configuration, allowing a wide, mode-hop free wavelength tunability. The ability to operate at room temperature and the overall laser compact size allow portable sensors to be developed.

While there are a number of gas sensing techniques employing laser sources, we will focus on gas sensors based on QEPAS, whose fundamentals and advantages have been discussed in Section 13.3.

13.4.1 Environmental Monitoring

Climate, human health, terrestrial and aquatic ecosystems, and agricultural productivity depend on atmospheric composition. Human activities have an increasing influence

on atmospheric composition, with subsequent environmental impacts [59]. Therefore, environmental trace gas monitoring is fundamental to assess human health risks in polluted urban or industrial surroundings, and to mitigate climate change caused by greenhouse gas emissions [60]. Directive 2008/50/EC of the European Parliament and of the Council of May 21, 2008 on ambient air quality and cleaner air for Europe established threshold values for the following pollutants: sulphur dioxide (SO_2), nitrogen oxides (NO_x), particulate matter (PM), lead (Pb), benzene (C_6H_6), and carbon monoxide (CO), due to their contributions to photochemical smog, acid rains, ozone depletion in the atmosphere, and troposphere ozone formation [61]. In addition, carbon dioxide (CO_2), methane (CH_4), and nitrous oxide (N_2O) must be monitored as the most important greenhouse gases [62].

Most of the environmentally relevant gas molecules as well as explosives and toxic gases exhibit strong absorption features in the mid-infrared spectral range. For this reason, spectroscopic techniques employing mid-infrared QCLs have been developed, aiming at high-sensitivity trace gas detection. In particular, QEPAS has been demonstrated as a powerful technique for harmful pollutant or greenhouse gas sensing. For example, a QEPAS sensor approach for the detection of triacetone triperoxide (TATP), a peroxide-based explosive, was presented for the first time in [63]. C-O stretch bands near 1200 cm^{-1} are detected by employing a widely tunable pulsed external cavity QCL (EC-QCL), at a duty cycle of 5%, producing an average output power of 5 mW. The sensor architecture employs a QEPAS spectrophone in on-beam configuration. Starting from an amount of 500 μg of TATP synthesized ad hoc for the experiment, a concentration of 65 ppm at ambient air is detected, with a detection limit of 1 part per million ppm. Continuous wave EC-QCLs have been employed in off-beam QEPAS sensors for the detection of laboratory samples of nitrous acid in gas phase (HONO) and hydrogen sulphide (H_2S) in the $1254\text{--}1256\text{ cm}^{-1}$ and $1233\text{--}1235\text{ cm}^{-1}$ spectral regions, respectively, as reported in [64] and [65]. Interest on HONO detection rises from the central role it plays in the atmospheric oxidation capacity, which in turn significantly affects the regional air quality and the global climate change. With a laser output power of 50 mW and a lock-in integration time of 1 s, the authors report a minimum detection limit of 66 ppb by volume (ppbv). Hydrogen sulphide is a harmful gas and its occupational exposure limit is regulated. It is of essential importance to perform H_2S monitoring in the field of petrochemical and biotechnological processes. The reported sensitivity for 160 mW of QCL optical power, at 1 s lock-in time constant, is 492 ppbv.

Another example of a QCL-based QEPAS sensor targeting a gas molecule relevant for environmental monitoring is reported in [66]. Here, an array of 32 pulsed distributed-feedback QCLs emitting in the $1190\text{--}1340\text{ cm}^{-1}$ spectral range is employed as the excitation source of a quartz-enhanced photoacoustic sensor in on-beam configuration for nitrous oxide broadband detection. At a duty cycle of 0.75%, the highest average optical power measured between the 32-QCLs device is of 1.6 mW. With a 10 s lock-in integration time, a detection limit of less than 60 ppb is achieved, matching the sensitivity level required for nitrous oxide monitoring at global atmospheric levels.

13 QCL-based Gas Sensing with Photoacoustic Spectroscopy

427

The reviewed examples put solid basis on the development of QCL-based QEPAS sensors for environmental applications. Up to now, four in-field tested sensors have been developed, whose main characteristics are summarized in Table 13.2.

The first in-field test of a QEPAS sensor for environmentally relevant gas molecules monitoring was demonstrated in 2013 in [67]. Here, an on-beam spectrophone configuration and a high-power continuous wave distributed feedback (DFB) QCL emitting at $\sim 2169\text{ cm}^{-1}$ have been selected to develop a QEPAS sensor for carbon monoxide (CO) and nitrous oxide (N_2O) detection. By adding 2.6% water vapor concentration in the gas line and using a lock-in integration time of 1 s, the achieved minimum detection limit is of 1.5 ppbv at atmospheric pressure for CO and of 23 ppbv at 100 torr for N_2O . The sensor was first optimized and calibrated in the laboratory, by employing gas cylinders containing certified concentration of the two investigated gas species. Then, a continuous monitoring of atmospheric CO and N_2O concentration levels was performed by placing the inlet tube of the QEPAS sensor outside the laboratory, in the Rice University campus (Houston, TX, USA). The concentration levels of the two gases were monitored by locking the QCL emission wavelength to the CO absorption line for the first and a half hours, and then to the N_2O absorption line for the next five hours. The obtained results are shown in Fig. 13.6.

The measured N_2O atmospheric concentration level is relatively stable, while peaks in the CO concentration over a background of ~ 130 ppbv are measured when people smoke close to the sensor inlet (concentration over 750 ppbv) or automobiles pass through the campus road ~ 20 meters away from the sensor sampling inlet. When pure nitrogen is flushed through the gas line, the signal drops to zero, as can be observed in the final part of both data plots. Reliable and robust operation of the QEPAS sensor was thus demonstrated.

In 2019 an improved QEPAS sensor for CO detection in air, at atmospheric pressure, was reported [41]. Compared to the previous work, the employed laser source targeted the CO absorption line at 2169.2 cm^{-1} with an optical power ~ 50 times lower. However, the use of an optimized spectrophone allowed comparable sensitivity levels to be achieved. The sensor was calibrated in the laboratory and tested for in-field measurements. Seven-days continuous measurements were implemented by placing

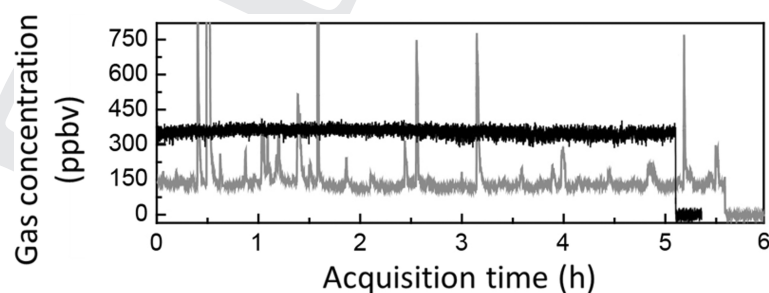


Fig. 13.6 Atmospheric CO (grey line) and N_2O (black line) concentration levels measured from air sampled at Rice University campus, Houston, TX, USA. The two tracks were acquired in succession.

Table 13.2 List of gas molecules detected in air by employing a QCL-based QEPAS sensor for environmental monitoring purposes. For each molecule, the QCL configuration (DFB – distributed feedback), operation (cw – continuous wave), emission wavenumber, and optical power (P) are reported, as well as the QEPAS sensor configuration, operating pressure, achieved sensitivity at 1 s lock-in integration time (i.t.), and the sensor field-test location.

Gas molecule	QCL config. and op.	Wavenumber (cm^{-1})	P (mW)	QEPAS config.	Pressure (torr)	Sensitivity at 1 s i.t. (ppbv)	Field-test location	Ref.
CO	DFB, cw	2169.2	987	On-beam	760	(+H ₂ O 2.6%) 1.5	Rice University campus, Houston, TX, USA	[67]
	DFB, cw	2169.2	21	On-beam	700	(+H ₂ O 2.5%) 7	Shanxi University, Taiyuan, China	[41]
	DFB, cw	2169.6	987	On-beam	100	(+H ₂ O 2.6%) 23	Rice University campus, Houston, TX, USA	[67]
N ₂ O	DFB, cw	1275.49	120	On-beam	130	6	BFI McCarty landfill, Houston, TX, USA	[68]
CH ₄	DFB, cw	1275.04	120	On-beam	130	13	BFI McCarty landfill, Houston, TX, USA	[68]
NO	DFB, cw	1900.07	65	Off-beam	760	120	Chinese University of Hong Kong, Hong Kong	[69]

the sensor out of the Yifu building of Shanxi University, China, to verify the reliability and validity of the developed system. The obtained data well-matched the one recorded by a China National Environmental Monitoring Center monitoring station, 7 km away from the campus.

In 2014 a compact QCL-based on-beam QEPAS sensor for environmental monitoring of greenhouse gases was developed [68]. A continuous wave DFB-QCL was employed to excite the CH_4 and N_2O absorption lines at 1275.04 cm^{-1} and 1275.49 cm^{-1} , respectively, with an optical power of 120 mW. For a working pressure of 130 torr and a lock-in integration time of 1 s, detection limits of 13 ppbv and 6 ppbv were achieved, respectively. Laboratory measurements aiming at proving the sensor stability and reproducibility were performed. The sensor was later installed in the Aerodyne Research, Inc. mobile laboratory for atmospheric CH_4 and N_2O sensing at the BFI McCarty landfill, an urban solid waste disposal site in the Greater Houston area. Measurements revealed high CH_4 concentration levels, up to 27 ppm by volume (ppmv), confirmed by the values measured by a multi-pass absorption cell-based sensor installed in a van.

Another air pollutant sensor based on the QEPAS technique was reported in 2017 in [69]. A compact and sensitive mid-infrared nitric oxide (NO) sensor was designed by using a distributed-feedback QCL emitting at 1900.07 cm^{-1} with an optical power of 65 mW and a spectrophone in off-beam configuration. With a minimum detection limit of 120 ppbv, for a lock-in integration time of 1 s, the QEPAS NO sensor was deployed in real-time diesel-engine exhaust monitoring. Measurements were performed by sampling the exhaust of a ISUZU LT 134L bus diesel engine (6HK1-TC Euro-III Compliant Rear Engine) at the Chinese University of Hong Kong. A slight decrease of the QEPAS signal was observed due to soot scattering the laser light, highlighting the importance of integrating a soot filter at the sensor inlet. An increase of NO concentrations from 126 ppmv to 187 ppmv in the exhaust was measured when engine rotational speed increased from 500 to 2000 revolutions per minute.

13.4.2 Breath Analysis

Human breath is composed of a matrix of nitrogen, oxygen, water vapor, carbon dioxide and inert gases (Ar, Ne, He), where a mixture of as many as 500 molecules is diluted in traces concentrations. Such a composition is determined by the inspiratory air and the volatile organic compounds present in the blood, which are originated by molecules and their metabolites that are (i) inhaled, (ii) absorbed by skin, (iii) ingested, and (iv) produced by tissues and cells in the body [70]. The presence of some molecules or metabolites in the exhaled molecular profile, in elevated concentrations compared to the normal ones, is closely associated with inflammatory processes and diseases [71]. For example, kidney and liver dysfunction lead to high levels of ammonia (NH_3) in breath [72], diabetes causes an increase of acetone ($\text{C}_3\text{H}_6\text{O}$) [73], asthma and upper respiratory track inflammation cause high levels of nitric oxide (NO) [74], and neonatal icterus leads to a carbon monoxide (CO) concentration increase [75]. Therefore, breath analysis has an enormous potential for clinical applications

aiming at early disease diagnosis and screening. Moreover, compared to other diagnostic techniques (e.g., histologic examination), breath sampling is non-invasive, safe for the patient, painless, and can be performed, if necessary, multiple times, at any site (laboratory, operation room, bedside) and over a large number of subjects.

Despite its undeniable potential, clinical breath analysis is still in its infancy and just a few molecules and metabolites breath tests have been approved by national public health institutions, mainly due to the stringent requirements on sampling procedures and measurements reproducibility [76].

In the last decade, the characteristics of laser-based spectroscopy, as summarized in Table 13.1, have and, in particular, of QEPAS, as described in Section 13.3, have lead researchers to develop QCL-based QEPAS sensors for potential breath sensing application. Indeed, the high-power (compared to diode lasers and interband cascade lasers) narrow linewidth emission of QCLs, combined with the performance of the QEPAS spectrophones and with the selection of the best operating pressure, provide the selectivity and sensitivity levels required to avoid false positives and false negatives in the breath analysis. For example, in [77] a QEPAS sensor for ethylene (C_2H_4) detection is reported, employing a continuous wave DFB-QCL, emitting at 967.40 cm^{-1} with an optical power of 74.2 mW, and an optimized spectrophone in on-beam configuration. The best working pressure for interferents-isolated, high-sensitivity C_2H_4 detection is found to be 120 torr. At 10 s lock-in integration time, a sensitivity of 10 ppb is achieved, comparable to the C_2H_4 concentration levels in breath indicative of lipid peroxidation in lung epithelium. Another example is reported in [78], where a continuous wave DFB-QCL emitting at 2178.69 cm^{-1} with an optical power of 75 mW is employed in an on-beam QEPAS sensor to detect carbon disulphide (CS_2), a biomarker of respiratory bacterial colonization in cystic fibrosis. Here, a minimum detection limit of 28 ppbv is achieved for a lock-in integration time of 1 s when the gas sample is moisturized with a water vapor concentration of 2.3 vol%, to improve the gas vibrational-translational relaxation process, at a pressure of 56 torr. In [33] a widely tunable, mode-hop-free EC-QCL is employed in a QEPAS sensor in on-beam configuration for nitric oxide detection at 1900.08 cm^{-1} with 66 mW optical excitation power. Here, a NO detection sensitivity of 4.9 ppbv is achieved with a 1 s lock-in integration time, by adding a 2.5% of water vapor concentration, at 250 torr. In the abovementioned three examples, measurements are performed by employing cylinders containing a certified concentration of the target gas, later diluted with nitrogen (and, in some cases, also water vapor). A further step toward a clinical breath sensing application is proposed in [79], where the EC-QCL is replaced with a $\sim 100\text{ mW}$ DFB-QCL emitting at 1900.08 cm^{-1} , in order to reduce the setup size and realize a compact and portable sensor with a comparable sensitivity. By employing the sensor described in [79], a preliminary breath-test was performed by measuring the airway wall nitric oxide concentration exhaled by four volunteers. This test was performed in Rice University, Houston, TX, USA. In Fig. 13.7 the volunteers' exhaled NO QEPAS signal (labels: v.A, v.B, v.C, v.D) is reported and compared with the signal measured for a certified reference N_2 gas mixture containing 95 ppb of NO concentration and a water vapor concentration of 2.5 vol%. The whole measurement was performed by locking

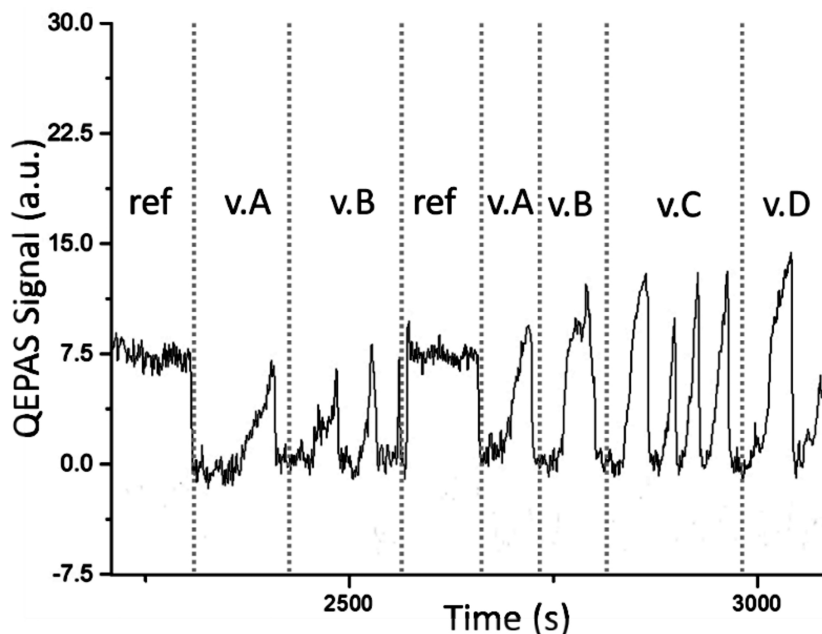


Fig. 13.7 QEPAS signal amplitude of a mixture of 95 ppb of NO, 2.5% H₂O, rest N₂ (ref), and of breath samples from four volunteers (v.A, v.B, v.C, v.D), obtained by locking the QCL emission wavenumber to the NO absorption line.

the laser emission wavenumber to the nitric oxide absorption line at 1900.08 cm^{-1} . The gas line inlet allows for switching between the reference gas mixture and a breath collector.

Each time the inlet is switched from the mixture containing a known concentration of NO to the breath collector, the signal quickly drops to zero till the volunteer starts breathing. The NO breath signal changes for each volunteer, depending on breath duration, mouth pressure, and NO concentration, while the QEPAS signal measured between 2550 s and 2680 s is the same as the one measured in the first part of the acquired track. All these characteristics prove a complete absence of any memory or saturation effect. Moreover, the signal resembles the breath dynamic of the volunteer, due to the fast response time of the sensor.

The work presented in [79] provides a proof-of-concept on the potential of QCL-based QEPAS as a powerful breath sensing technique. The first clinical study of a QEPAS-based breath sensor was performed at the St. Luke's University Hospital of Bethlehem, PA, USA, in 2013 [80]. In this study, breath ammonia is detected with a fast, real-time monitor using a continuous wave DFB-QCL-based on-beam QEPAS sensor coupled to a breath sampling device that measures mouth pressure and the real-time concentration of carbon dioxide. The selected laser source allows the 967.35 cm^{-1} NH₃ absorption line to be targeted with an optical power of 24 mW. At a working pressure of 120 torr a detection sensitivity as low as six ppbv is achieved with a 1 s lock-in integration time. The NH₃ QEPAS sensor was used to evaluate potential

clinical utility of breath ammonia compared to blood ammonia. In particular, a protocol was used to study the effects that the mode of breathing and the mouth pH have on the determination of exhaled breath ammonia. In 2015, the same breath ammonia sensor was employed to evaluate ammonia physiology in healthy and cirrhotic adults [81].

Recently, the first carbon monoxide sensor dedicated to human breath analysis, based on QEPAS, was tested at the Montpellier University Hospital, Montpellier, France [82]. The developed sensor employed a continuous wave Fabry–Pérot QCL emitting at 2103.26 cm^{-1} (targeting CO absorption line) with an optical power of 80 mW and a spectrophone in the off-beam configuration. The achieved sensitivity at atmospheric pressure, at a lock-in integration time of 1 s is 20 ppbv. The performance of the QEPAS sensor was compared with reference methods. The obtained results confirmed the ability of the QCL-based QEPAS sensor for measuring low-level endogenous exhaled CO concentrations.

The characteristics of the three described QCL-based QEPAS sensors targeting biomarkers in exhaled breath are summarized in Table 13.3.

13.4.3 Leak Detection

Leak detection and localization plays an important role in mechatronics, biotechnology, petrochemical and automotive industries, and all the industrial fields requiring manufacturing quality-control processes [83]. In contrast to other control tests, leak detection employs techniques which do not damage the characteristics or performances of components like vessels, valves, pipes, or rubber seals [84, 85].

In 2016, a leak detector based on QEPAS technique was developed to test mechatronics systems and components, such as vacuum-valves and diesel injectors, usually operating at high pressures [86]. Leak tightness requirements are extremely important in automotive industry to lower emissions and improve fuel consumption. The sensor employed sulfur hexafluoride (SF_6) as a leak tracer gas due to being an extremely stable, inert, non-flammable, and non-toxic, gas, making it particularly suitable and safe for working-environment use [87]. A QCL in external-cavity configuration, resonant with a strong SF_6 absorption band around 947 cm^{-1} , was employed as the excitation source. The QEPAS sensor was integrated in a vacuum-sealed test station. Validation tests showed a minimum detection sensitivity of 2.75 ppb for a 1 s integration time, corresponding to a minimum detectable leak of $4.5 \cdot 10^{-7}$ mbar·l/s, for a nitrogen gas carrier flow of 0.67 mbar·l/s. If pure SF_6 is used as leak test gas, the sensitivity can be improved down to $\sim 4.5 \cdot 10^{-9}$ mbar·l/s. In terms of sensitivity, QEPAS is competitive with most of the techniques reported in literature [88], some of which are listed in Table 13.4. However, compared with these techniques, QEPAS is the only one also combining the characteristics of short response time, compactness, low weight and cost, and safety [86].

13.4.4 Multi-Gas Detection

Isotopes concentration ratio measurements, molecular relaxation dynamics studies, industrial process control, as well as the aforementioned environmental monitoring

Table 13.3 The list of breath biomarkers detected by employing QCL-based QEPAS sensors. For each molecule, the QCL configuration (DFB – distributed feedback, FP – Fabry–Pérot), operation (cw – continuous wave), emission wavenumber, and optical power (P) are reported, as well as the QEPAS sensor configuration, operating pressure, and achieved sensitivity at 1 s lock-in integration time (i.t.), as well as the sensor field-test location.

Gas molecule	QCL config. and op.	Wavenumber (cm^{-1})	P (mW)	QEPAS config.	Pressure (torr)	Sensitivity at 1 s i.t. (ppbv)	Field-test location	Ref.
NO	DFB, cw	1900.08	60	On-beam	250	(+H ₂ O 2.5%) 4	Rice University campus, Houston, TX, USA	
NH ₃	DFB, cw	967.35	24	On-beam	120	6	(proof of concept) St. Luke's University Hospital, Bethlehem, PA, USA	[79]
CO	FP, cw	2103.26	80	Off-beam	760	20	Montpellier University Hospital, Montpellier, France	[80] [82]

Table 13.4 List of the main leak detection methods and corresponding sensitivity levels.

Leak detection technique	Sensitivity (mbar·l/s)
QEPAS	10^{-9}
Bubble in water	10^{-2}
Vacuum decay	10^{-3}
Halogen detector	10^{-6}
Radio-isotope	10^{-10}
Mass spectroscopy	10^{-11}

and breath biomarkers detection are some of the sensing applications requiring detection and quantification of different components in a gas mixture, simultaneously or quasi-simultaneously [89]. With this purpose, several on-beam QEPAS sensors have been developed, whose characteristics, in terms of analyzed gas mixture, employed QCL source features, and possible applications, are summarized in Table 13.5.

In [90], the dynamic range of a continuous wave distributed-feedback QCL was exploited to selectively detect isotopes $^{12}\text{CH}_4$ and $^{13}\text{CH}_4$ in methane samples at the natural abundance, in the $1296.00\text{--}1296.15\text{ cm}^{-1}$ spectral range. Isotopic ratio can be used as both fingerprint and indicator for many processes involving isotopic fractionations. The thermogenic or biogenic origin of natural gas, as well as its source and history, can be identified by measuring the methane isotopic ratio. Therefore, with a sensitivity at the parts-per-billion level, this sensor opens the way to the development of QEPAS-based gas spectrometers to be employed downhole for oil and gas exploration. The cw DFB-QCL-based QEPAS sensor demonstrated in [91] has a great potential for both breath pattern recognition and environmental monitoring. Indeed, this sensor detects ethylene and carbon dioxide, which are both biomarkers and pollutant gases, in the $949.1\text{--}949.6\text{ cm}^{-1}$ spectral range, and provides a study of the influence of the CO_2 addition to the $\text{C}_2\text{H}_4/\text{N}_2$ mixture on the photoacoustic signal of ethylene, supported by the development of an energy transfer model in the analyzed gas mixture. Environmental monitoring is also the possible field of application of the dual-gas sensors described in [92] and [93]. In the first case, a $\text{CO-N}_2\text{O}$ sensor is developed by employing a cw DFB-QCL. In the second case, detection of chlorodifluoromethane (CHClF_2) and acetone ($\text{C}_3\text{H}_6\text{O}$) is demonstrated in the $1180\text{--}1345\text{ cm}^{-1}$ spectral region by exploiting the tunability range of an external cavity QCL. In this last example, each target molecule exhibits unresolved rotational–vibrational absorption lines. However, the absorption features of the two molecules lay in different spectral regions. When the strong absorption features of the target molecules overlap, multi-gas sensing becomes challenging.

The first strongly overlapped, broadband absorbing molecules QEPAS detection is reported in [94]. A widely tunable mode-hop free external cavity QCL is used to target the absorption lines of pentafluoroethane (Freon 125, C_2HF_5) and acetone in the spectral range from 1127 cm^{-1} to 1245 cm^{-1} . QEPAS reference spectra of the single-gas

Table 13.5 List of gas mixtures detected by employing a QCL-based on-beam QEPAS sensor. For each mixture, the gas components concentration is reported and the spectral overlap (Ov.) of absorption features of different molecules is specified. The employed QCL configuration (DFB – distributed feedback, EC – external cavity), operation (cw – continuous wave), emission wavenumber range, and average optical power are reported, together with the sensing application (BS – breath sensing, EM – environmental monitoring).

Gas mixture	Analysed gas components concentration	Ov.	QCL config. and op.	Wavenumber range (cm ⁻¹)	Optical power (mW)	Possible application	Ref.
¹² CH ₄ – ¹³ CH ₄	49.41 ppm – 0.555 ppm	no	DFB, cw	1296–1296.15	~112	Oil and gas exploration	[90]
C ₂ H ₄ –CO ₂	9 ppm – 1%	no	DFB, cw	949.1–949.6	~16	BS, EM	[91]
CO–N ₂ O	250 ppm – 750 ppm	no	DFB, cw	2188.8–2191.2	~75	EM	[92]
CHClF ₂ –C ₃ H ₆ O	1.32% – 0.96%	no	EC, pulsed	1180–1345	~2	EM	[93]
C ₂ HF ₅ –C ₃ H ₆ O	4.4 ppm – 47.2 ppm	yes	EC, cw	1127–1245	~6.6	Broadband spectroscopy	[94]
CH ₄ –N ₂ O	150 ppm – 510 ppm	yes	DFB QCL array, pulsed	1190–1340	~1.6	EM	[95]
C ₂ H ₂ –CH ₄ –N ₂ O	150 ppm – 3000 ppm – 550 ppm	yes	DFB, cw	1295.5–1296.5	~112	EM	[92]

species are first acquired separately. Then, the QEPAS spectrum recorded for a gas mixture with an unknown concentration of both species is fitted by a linear combination of the reference spectra. A similar approach is adopted in [95], where broadband detection of mixtures of N_2O and CH_4 in dry nitrogen is demonstrated by using an array of 32 DFB-QCLs having an emission in the spectral range between 1190 cm^{-1} and 1340 cm^{-1} . Despite the significant overlap in the target gas molecules absorption spectra, determination of nitrous oxide and methane concentrations is demonstrated, representing a starting point for the development of sensors aiming at environmental monitoring of broadband greenhouse gases. However, linear regression is efficient as long as the experimental data are uncorrelated or at least weakly correlated; otherwise, a lack of precision and accuracy can occur [96]. For this reason, an algorithm based on partial least squares regression is employed in [92] to retrieve the components concentration in a three-gas mixture. Here, a cw DFB QCL is employed as the excitation source of a QEPAS sensor for environmentally relevant gas detection. Analyzed gas mixtures are composed of different amounts of acetylene (C_2H_2), methane, and nitrous oxide, showing a spectral overlap greater than 97% in the laser emission range ($1295.5\text{--}1296.5\text{ cm}^{-1}$). The calibration error reported for the three-gas components concentrations predicted by PLSR tool is up to five times better, compared with standard linear regression.

13.5 Conclusion

This chapter presents an overview of the gas sensors based on quartz-enhanced photoacoustic spectroscopy employing quantum cascade lasers as the excitation light source. Optical gas sensing techniques are sensitive, non-destructive tools to detect gas species in situ and in real time. In particular, photoacoustic spectroscopy and quartz-enhanced photoacoustic spectroscopy, whose physical principles are described in Sections 13.2 and 13.3, combined with the advantages of quantum cascade lasers, have been exploited to develop high-sensitivity, compact, robust, portable, multi-gas detectors. QCL-based QEPAS sensors have been demonstrated for several applications, such as environmental monitoring, breath analysis, leak detection, and multi-gas detection, as reviewed in Section 13.4, thus demonstrating the versatility and great potential of the QCL-based QEPAS technique in gas sensing.

References

- [1] P. T. Moseley, "Solid state gas sensors," *Meas. Sci. Technol.*, vol. 8, no. 3, pp. 223–237, 1997.
- [2] N. Yamazoe and K. Shimano, "Receptor function and response of semiconductor gas sensor," *J. Sensors*, vol. 875704, 2009.
- [3] J. Hodgkinson and R. P. Tatam, "Optical gas sensing: A review," *Meas. Sci. Technol.*, vol. 24, no. 1, p. 012004, 2013.
- [4] A. Elia, P. M. Lugarà, C. Di Franco, and V. Spagnolo, "Photoacoustic techniques for trace gas sensing based on semiconductor laser sources," *Sensors*, vol. 9, pp. 9616–9628, 2009.

13 QCL-based Gas Sensing with Photoacoustic Spectroscopy

437

- [5] T. Tomberg, M. Vainio, T. Hieta, and L. Halonen, "Sub-parts-per-trillion level sensitivity in trace gas detection by cantilever-enhanced photo-acoustic spectroscopy," *Sci. Rep.*, vol. 8, p. 1848, 2018.
- [6] S. Manohar and D. Razansky, "Photoacoustics: a historical review," *Adv. Opt. Photon.*, Vol. 8, pp. 586–617, 2016.
- [7] L. Y. Hao *et al.*, "A new cylindrical photoacoustic cell with improved performance," *Rev. Sci. Instrum.*, vol. 73, no. 2 I, p. 404, 2002.
- [8] K. Song *et al.*, "Differential Helmholtz resonant photoacoustic cell for spectroscopy and gas analysis with room-temperature diode lasers," *Appl. Phys. B Lasers Opt.*, vol. 75, no. 2–3, pp. 215–227, 2002.
- [9] F. G. C. Bijnen, J. Reuss, and F. J. M. Harren, "Geometrical optimization of a longitudinal resonant photoacoustic cell for sensitive and fast trace gas detection," *Rev. Sci. Instrum.*, vol. 67, no. 8, pp. 2914–2923, 1996.
- [10] K. Wilcken and J. Kauppinen, "Optimization of a microphone for photoacoustic spectroscopy," *Appl. Spectrosc.*, vol. 57, no. 9, pp. 1087–1092, 2003.
- [11] D. C. Dumitras, D. C. Dutu, C. Matei, A. M. Magureanu, M. Petrus, and C. Popa, "Laser photoacoustic spectroscopy: Principles, instrumentation, and characterization," *J. Optoelectron. Adv. Mater.*, vol. 9, no. 12, pp. 3655–3701, 2007.
- [12] A. Miklós and A. Lörincz, "Windowless resonant acoustic chamber for laser-photoacoustic applications," *Appl. Phys. B Photophysics Laser Chem.*, vol. 48, no. 3, pp. 213–218, 1989.
- [13] Z. Yu *et al.*, "Aerosol Science and Technology Differential photoacoustic spectroscopic (DPAS)-based technique for PM optical absorption measurements in the presence of light absorbing gaseous species Differential photoacoustic spectroscopic (DPAS)-based technique for PM optical absorption measurements in the presence of light absorbing gaseous species," *Aerosol Sci. Technol.*, vol. 51, pp. 1438–1447, 2017.
- [14] O. E. Bonilla-Manrique, J. E. Posada-Roman, J. A. Garcia-Souto, and M. Ruiz-Llata, "Sub-ppm-level ammonia detection using photoacoustic spectroscopy with an optical microphone based on a phase interferometer," *Sensors*, vol. 19, no. 13, p. 2890, 2019.
- [15] N. A. Hall, M. Okandan, R. Littrell, B. Bicen, and F. L. Degertekin, "Micromachined optical microphone structures with low thermal-mechanical noise levels," *J. Acoust. Soc. Am.*, vol. 122, no. 4, pp. 2031–2037, 2007.
- [16] T. Kuusela and J. Kauppinen, "Photoacoustic gas analysis using interferometric cantilever microphone," *Appl. Spectrosc. Rev.*, vol. 42, no. 5, pp. 443–474, 2007.
- [17] A. Berrou, M. Raybaut, A. Godard, and M. Lefebvre, "High-resolution photoacoustic and direct absorption spectroscopy of main greenhouse gases by use of a pulsed entangled cavity doubly resonant OPO," *Appl. Phys. B Lasers Opt.*, vol. 98, no. 1, pp. 217–230, 2010.
- [18] S. D. Campbell, S. S. Yee, and M. A. Fromowitz, "Applications of photoacoustic spectroscopy to problems in dermatology research," *IEEE Trans. Biomed. Eng.*, vol. BME-26, no. 4, pp. 220–227, 1979.
- [19] F. J. M. Harren *et al.*, "On-line laser photoacoustic detection of ethene in exhaled air as biomarker of ultraviolet radiation damage of the human skin," *Appl. Phys. Lett.*, vol. 74, no. 12, pp. 1761–1763, 1999.
- [20] C. Fischer, R. Bartlome, and M. W. Sigris, "The potential of mid-infrared photoacoustic spectroscopy for the detection of various doping agents used by athletes," *Appl. Phys. B Lasers Opt.*, vol. 85, no. 2–3, pp. 289–294, 2006.

- [21] P. Patimisco, G. Scamarcio, F. K. Tittel, and V. Spagnolo, "Quartz-enhanced photoacoustic spectroscopy: A review," *Sensors*, vol. 14, pp. 6165–6206, 2014.
- [22] P. Patimisco, A. Sampaolo, L. Dong, F. K. Tittel, and V. Spagnolo, "Recent advances in quartz enhanced photoacoustic sensing," *Appl. Phys. Rev.*, vol. 5, no. 1, p. 011106, 2018.
- [23] A. A. Kosterev, F. K. Tittel, D. V. Serebryakov, A. L. Malinovsky, and I. V. Morozov, "Applications of quartz tuning forks in spectroscopic gas sensing," *Rev. Sci. Instrum.*, vol. 76, no. 4, p. 043105, 2005.
- [24] F. K. Tittel *et al.*, "Analysis of overtone flexural modes operation in quartz-enhanced photoacoustic spectroscopy," *Opt. Express*, Vol. 24, pp. A682–A692, 2016.
- [25] G. Wysocki, A. A. Kosterev, and F. K. Tittel, "Influence of molecular relaxation dynamics on quartz-enhanced photoacoustic detection of CO₂ at $\lambda = 2 \mu\text{m}$," *Appl. Phys. B Lasers Opt.*, vol. 85, no. 2–3, pp. 301–306, 2006.
- [26] L. Landau, "Theory of sound dispersion," *Phys. Zeitschrift der Sowjetunion*, vol. 10, pp. 34–43, 1936.
- [27] S. Schilt, J. P. Besson, and L. Thévenaz, "Near-infrared laser photoacoustic detection of methane: The impact of molecular relaxation," *Appl. Phys. B Lasers Opt.*, vol. 82, no. 2 SPEC. ISS., pp. 319–329, 2006.
- [28] P. Patimisco *et al.*, "Analysis of the electro-elastic properties of custom quartz tuning forks for optoacoustic gas sensing," *Sensors Actuators, B Chem.*, vol. 227, pp. 539–546, 2016.
- [29] A. Sampaolo *et al.*, "Improved tuning fork for terahertz quartz-enhanced photoacoustic spectroscopy," *Sensors (Switzerland)*, vol. 16, no. 4, p. 439, 2016.
- [30] P. Patimisco, A. Sampaolo, H. Zheng, L. Dong, F. K. Tittel, and V. Spagnolo, "Quartz-enhanced photoacoustic spectrophones exploiting custom tuning forks: A review," *Adv. Phys. X*, vol. 2, no. 1, pp. 169–187, 2017.
- [31] P. Patimisco *et al.*, "Tuning forks with optimized geometries for quartz-enhanced photoacoustic spectroscopy," *Opt. Express*, vol. 27, no. 2, p. 1401, 2019.
- [32] A. A. Kosterev, Y. A. Bakhrin, and F. K. Tittel, "Ultrasensitive gas detection by quartz-enhanced photoacoustic spectroscopy in the fundamental molecular absorption bands region," *Appl. Phys. B Lasers Opt.*, vol. 80, no. 1, pp. 133–138, 2005.
- [33] L. Dong, V. Spagnolo, R. Lewicki, and F. K. Tittel, "Ppb-level detection of nitric oxide using an external cavity quantum cascade laser based QEPAS sensor," *Opt. Express*, vol. 19, no. 24, p. 24037, 2011.
- [34] A. Elefante *et al.*, "Environmental monitoring of methane with quartz-enhanced photoacoustic spectroscopy exploiting an electronic hygrometer to compensate the H₂O influence on the sensor signal," *Sensors*, Vol. 20, 2935, 2020.
- [35] P. Patimisco *et al.*, "A quartz enhanced photo-acoustic gas sensor based on a custom tuning fork and a terahertz quantum cascade laser," *Analyst*, vol. 139, no. 9, pp. 2079–2087, 2014.
- [36] P. Patimisco *et al.*, "Octupole electrode pattern for tuning forks vibrating at the first overtone mode in quartz-enhanced photoacoustic spectroscopy," *Opt. Lett.*, vol. 43, no. 8, p. 1854, 2018.
- [37] M. Christen, "Air and gas damping of quartz tuning forks," *Sensors and Actuators*, vol. 4, no. C, pp. 555–564, 1983.
- [38] W. K. Blake, "The radiation from free-free beams in air and in water," *J. Sound Vib.*, vol. 33, no. 4, pp. 427–450, 1974.
- [39] P. Patimisco *et al.*, "Loss mechanisms determining the quality factors in quartz tuning forks vibrating at the fundamental and first overtone modes," *IEEE Trans. Ultrason. Ferroelectr. Freq. Control*, vol. 65, no. 10, pp. 1951–1957, 2018.

13 QCL-based Gas Sensing with Photoacoustic Spectroscopy

439

- [40] M. Giglio *et al.*, “Damping mechanisms of piezoelectric quartz tuning forks employed in photoacoustic spectroscopy for trace gas sensing,” *Phys. Status Solidi Appl. Mater. Sci.*, vol. 216, no. 3, p. 1800552, 2019.
- [41] S. Li *et al.*, “Ppb-level quartz-enhanced photoacoustic detection of carbon monoxide exploiting a surface grooved tuning fork,” *Anal. Chem.*, vol. 91, no. 9, pp. 5834–5840, 2019.
- [42] F. Sgobba *et al.*, “Quartz-enhanced photoacoustic detection of ethane in the near-IR exploiting a highly performant spectrophone,” *Appl. Sci.*, vol. 10, p. 2447, 2020.
- [43] Y. Ma *et al.*, “Ultra-high sensitive trace gas detection based on light-induced thermoelastic spectroscopy and a custom quartz tuning fork,” *Appl. Phys. Lett.*, vol. 116, no. 1, p. 011103, 2020.
- [44] B. Sun *et al.*, “Mid-infrared quartz-enhanced photoacoustic sensor for ppb-level CO detection in a SF₆ gas matrix exploiting a T-grooved quartz tuning fork,” *Anal. Chem.*, vol. 92, no. 16, pp. 13922–13929, 2020.
- [45] M. Relaxation and W. H. Flygare, “Molecular relaxation,” *Acc. Chem. Res.*, vol. 1, no. 4, pp. 121–127, 1968.
- [46] H. Zheng *et al.*, “Double antinode excited quartz-enhanced photoacoustic spectrophone,” *Appl. Phys. Lett.*, vol. 110, no. 2, p. 021110, 2017.
- [47] H. Hosaka, K. Itao, and S. Kuroda, “Damping characteristics of beam-shaped micro-oscillators,” *Sensors Actuators, A Phys.*, vol. 49, no. 1–2, pp. 87–95, 1995.
- [48] Y. Jimbo and K. Itao, “Energy loss of a cantilever vibrator,” *J. Horol. Inst. Japan*, no. 47, pp. 1–15, 1968.
- [49] D. M. Photiadis and J. A. Judge, “Attachment losses of high Q oscillators,” *Appl. Phys. Lett.*, vol. 85, no. 3, pp. 482–484, 2004.
- [50] K. Liu, X. Guo, H. Yi, W. Chen, W. Zhang, and X. Gao, “Off-beam quartz-enhanced photoacoustic spectroscopy,” *Opt. Lett.*, vol. 34, no. 10, p. 1594, 2009.
- [51] S. Böttger, M. Köhring, U. Willer, and W. Schade, “Off-beam quartz-enhanced photoacoustic spectroscopy with LEDs,” *Appl. Phys. B Lasers Opt.*, vol. 113, no. 2, pp. 227–232, 2013.
- [52] S. Dello Russo *et al.*, “Acoustic coupling between resonator tubes in quartz-enhanced photoacoustic spectrophones employing a large prong spacing tuning fork,” *Sensors (Switzerland)*, vol. 19, no. 19, 2019.
- [53] N. Ogawa and F. Kaneko, “Open end correction for a flanged circular tube using the diffusion process,” *Eur. J. Phys.*, vol. 34, no. 5, pp. 1159–1165, 2013.
- [54] F. G. Kitson, B. S. Larsen, and C. N. McEwen, *Gas Chromatography and Mass Spectrometry*. Burlington, MA: Academic Press, 1996.
- [55] R. E. Kirk, D. F. Othmer, M. Grayson, and D. Eckroth, *Kirk-Othmer Concise Encyclopedia of Chemical Technology*. Chichester: Wiley, 1985.
- [56] X. Giraud, N. N. Le-Dong, K. Hogben, and J. B. Martinot, “The measurement of DLNO and DLCO: A manufacturer’s perspective,” *Respir. Physiol. Neurobiol.*, vol. 241, pp. 36–44, 2017.
- [57] T. H. Risby and F. K. Tittel, “Current status of midinfrared quantum and interband cascade lasers for clinical breath analysis,” *Opt. Eng.*, vol. 49, no. 11, p. 111123, 2010.
- [58] J. Faist, F. Capasso, D. L. Sivco, C. Sirtori, A. L. Hutchinson, and A. Y. Cho, “Quantum cascade laser,” *Science (80-.)*, vol. 264, no. 5158, pp. 553–556, 1994.
- [59] World Meteorological Organization, *WMO Global Atmosphere Watch (GAW) Implementation Plan: 2016–2023*. 2018.

- [60] P. M. Hundt *et al.*, “Multi-species trace gas sensing with dual-wavelength QCLs,” *Appl. Phys. B Lasers Opt.*, vol. 124, no. 6, p. 108, 2018.
- [61] “Directive 2008/50/EC of the European Parliament and of the Council of 21 May 2008 on ambient air quality and cleaner air for Europe,” *Off. J. Eur. Union*, 2008.
- [62] B. V. Braatz and S. Barvenik, “National greenhouse gas emission inventories in developing countries and countries with economies in transition: Global synthesis,” in *Greenhouse Gas Emission Inventories: Interim Results from the U.S. Country Studies Program*, B. V. Braatz, B. P. Jallow, S. Molnár, D. Murdiyarsa, M. Perdomo, and J. F. Fitzgerald, Eds. Dordrecht: Springer Netherlands, 1996, pp. 1–57.
- [63] C. Bauer *et al.*, “A mid-infrared QEPAS sensor device for TATP detection,” *J. Phys. Conf. Ser.*, vol. 157, no. 1, 2009.
- [64] H. Yi, R. Maamary, X. Gao, M. W. Sigrist, E. Fertein, and W. Chen, “Short-lived species detection of nitrous acid by external-cavity quantum cascade laser based quartz-enhanced photoacoustic absorption spectroscopy,” *Appl. Phys. Lett.*, vol. 106, no. 10, p. 101109, 2015.
- [65] M. Helman, H. Moser, A. Dudkowiak, and B. Lendl, “Off-beam quartz-enhanced photoacoustic spectroscopy-based sensor for hydrogen sulfide trace gas detection using a mode-hop-free external cavity quantum cascade laser,” *Appl. Phys. B Lasers Opt.*, vol. 123, no. 5, p. 141, 2017.
- [66] M. Giglio *et al.*, “Nitrous oxide quartz-enhanced photoacoustic detection employing a broadband distributed-feedback quantum cascade laser array,” *Appl. Phys. Lett.*, vol. 113, no. 17, p. 171101, 2018.
- [67] Y. Ma, R. Lewicki, M. Razeghi, and F. K. Tittel, “QEPAS based ppb-level detection of CO and N₂O using a high power CW DFB-QCL,” *Opt. Express*, vol. 21, no. 1, pp. 1008–1019, 2013.
- [68] M. Jahjah *et al.*, “A compact QCL based methane and nitrous oxide sensor for environmental and medical applications,” *Analyst*, vol. 139, no. 9, pp. 2065–2069, 2014.
- [69] C. Shi *et al.*, “A mid-infrared fiber-coupled QEPAS nitric oxide sensor for real-time engine exhaust monitoring,” *IEEE Sens. J.*, vol. 17, no. 22, pp. 7418–7424, 2017.
- [70] K. H. Kim, S. A. Jahan, and E. Kabir, “A review of breath analysis for diagnosis of human health,” *TrAC – Trends in Analytical Chemistry*, vol. 33, pp. 1–8, 01, 2012.
- [71] C. Wang and P. Sahay, “Breath analysis using laser spectroscopic techniques: Breath biomarkers, spectral fingerprints, and detection limits,” *Sensors*, vol. 9, no. 10, pp. 8230–8262, 2009.
- [72] S. Davies, P. Spanel, and D. Smith, “Quantitative analysis of ammonia on the breath of patients in end-stage renal failure,” *Kidney Int.*, vol. 52, no. 1, pp. 223–228, 1997.
- [73] C. N. Tassopoulos, D. Barnett, and T. R. Fraser, “Breath-acetone and blood-sugar measurements in diabetes,” *Lancet*, vol. 293, no. 7609, pp. 1282–1286, 1969.
- [74] M. R. McCurdy, A. Sharafkhaneh, H. Abdel-Monem, J. Rojo, and F. K. Tittel, “Exhaled nitric oxide parameters and functional capacity in chronic obstructive pulmonary disease,” *J. Breath Res.*, vol. 5, no. 1, p. 016003, 2011.
- [75] H. Okuyama, M. Yonetani, Y. Uetani, and H. Nakamura, “End-tidal carbon monoxide is predictive for neonatal non-hemolytic hyperbilirubinemia,” *Pediatr. Int.*, vol. 43, no. 4, pp. 329–333, 2001.
- [76] A. Amann, P. Spanel, and D. Smith, “Breath analysis: the approach towards clinical applications,” *Mini-Reviews Med. Chem.*, vol. 7, no. 2, pp. 115–129, 2007.

- [77] M. Giglio *et al.*, “Quartz-enhanced photoacoustic sensor for ethylene detection implementing optimized custom tuning fork-based spectrophone,” *Opt. Express*, vol. 27, no. 4, pp. 4271–4280, Feb. 2019.
- [78] J. P. Wacławek, H. Moser, and B. Lendl, “Compact quantum cascade laser based quartz-enhanced photoacoustic spectroscopy sensor system for detection of carbon disulfide,” *Opt. Express*, vol. 24, no. 6, p. 6559, 2016.
- [79] R. Lewicki, L. Dong, Y. Ma, and F. K. Tittel, “A compact CW quantum cascade laser based QEPAS sensor for sensitive detection of nitric oxide,” in *CLEO: Science and Innovations, CLEO_SI 2012*, May 2012, p. CW3B.4.
- [80] S. F. Solga *et al.*, “Factors influencing breath ammonia determination,” *J. Breath Res.*, vol. 7, no. 3, 2013.
- [81] L. A. Spacek, M. Mudalel, F. Tittel, T. H. Risby, and S. F. Solga, “Clinical utility of breath ammonia for evaluation of ammonia physiology in healthy and cirrhotic adults,” *J. Breath Res.*, vol. 9, no. 4, p. 047109, 2015.
- [82] N. Maurin *et al.*, “First clinical evaluation of a quartz enhanced photo-acoustic CO sensor for human breath analysis,” *Sensors Actuators, B Chem.*, vol. 319, p. 128247, 2020.
- [83] L. Li, K. Yang, X. Bian, Q. Liu, Y. Yang, and F. Ma, “A gas leakage localization method based on a virtual ultrasonic sensor array,” *Sensors (Switzerland)*, vol. 19, no. 14, 2019.
- [84] O. M. Aamo, “Leak detection, size estimation and localization in pipe flows,” *IEEE Trans. Automat. Contr.*, vol. 61, no. 1, pp. 246–251, 2016.
- [85] Q. He, A. Li, Y. Zhang, S. Liu, Y. Guo, and L. Kong, “A study on mechanical and tribological properties of silicone rubber reinforced with white carbon black,” *Tribol. – Mater. Surfaces Interfaces*, vol. 12, no. 1, pp. 9–16, 2018.
- [86] A. Sampaolo *et al.*, “Highly sensitive gas leak detector based on a quartz-enhanced photoacoustic SF6 sensor,” *Opt. Express*, vol. 24, no. 14, p. 15872, 2016.
- [87] M. Maiss and C. A. M. Brenninkmeijer, “Atmospheric SF6: Trends, sources, and prospects,” *Environ. Sci. Technol.*, vol. 32, no. 20, pp. 3077–3086, 1998.
- [88] A. Pregelj, M. Drab, and M. Mozetic, “Leak detection methods and defining the sizes of leaks,” *Proc. 4th International Conference of Slovenian Society for Nondestructive Testing*, Ljubljana, Slovenia, 1997.
- [89] A. Elefante *et al.*, “Dual-gas quartz-enhanced photoacoustic Sensor for simultaneous detection of methane/nitrous oxide and water vapor,” *Anal. Chem.*, vol. 91, no. 20, pp. 12866–12873, 2019.
- [90] A. Sampaolo *et al.*, “Quartz-enhanced photoacoustic spectroscopy for hydrocarbon trace gas detection and petroleum exploration,” *Fuel*, vol. 277, p. 118118, 2020.
- [91] Z. Wang, J. Geng, and W. Ren, “Quartz-enhanced photoacoustic spectroscopy (QEPAS) detection of the ν_7 band of ethylene at low pressure with CO₂ interference analysis,” *Appl. Spectrosc.*, vol. 71, no. 8, pp. 1834–1841, 2017.
- [92] A. Zifarelli *et al.*, “Partial least-squares regression as a tool to retrieve gas concentrations in mixtures detected using quartz-enhanced photoacoustic spectroscopy,” *Anal. Chem.*, vol. 92, no. 16, 2020.
- [93] S. Zhou *et al.*, “External cavity quantum cascade laser-based QEPAS for chlorodifluoromethane spectroscopy and sensing,” *Appl. Phys. B Lasers Opt.*, vol. 125, no. 7, p. 125, 2019.
- [94] R. Lewicki *et al.*, “QEPAS based detection of broadband absorbing molecules using a widely tunable, cw quantum cascade laser at 8.4 μm ,” *Opt. Express*, Vol. 15, 7357–7366, 2007.

- [95] M. Giglio *et al.*, “Broadband detection of methane and nitrous oxide using a distributed-feedback quantum cascade laser array and quartz-enhanced photoacoustic sensing,” *Photoacoustics*, vol. 17, p. 100159, 2020.
- [96] S. Wold, A. Ruhe, H. Wold, and W. J. Dunn, III, “The collinearity problem in linear regression: The partial least squares (PLS) approach to generalized inverses,” *SIAM J. Sci. Stat. Comput.*, vol. 5, no. 3, pp. 735–743, 1984.